# X-ray diffraction study on residual stress and preferred orientation in thin titanium films subjected to a high ion flux during deposition

M. Birkholz[a)]
*Fraunhofer Institut für Schicht- und Oberflächentechnik Bienroder Weg 54 E, 38108 Braunschweig, Germany*

C. Genzel
*Hahn-Meitner-Institut, Bereich Strukturforschung, Albert Einstein Strasse 15, 12489 Berlin, Germany*

T. Jung
*Fraunhofer Institut für Schicht- und Oberflächentechnik Bienroder Weg 54 E, 38108 Braunschweig, Germany*

(Received 5 April 2004; accepted 16 September 2004)

The structural properties of thin Ti films were studied by x-ray scattering techniques aiming at an improved understanding of residual stress and preferred orientation in thin metal films when subjected to a high ion flux during deposition. The samples were prepared by gas-flow sputtering and by subjecting the substrate to a midfrequency bias during deposition. Large arrival ratios of ions over deposited atoms, $J_i/J_a$, could be realized by this processing. Some hundred nanometers thin Ti layers were characterized by x-ray reflectometry, symmetric $\theta/2\theta$ diffraction, pole figure analysis, and residual stress measurements by the $\sin^2\psi$ and by the scattering vector technique, the latter method enabling a depth-resolved determination of stress fields. Whereas the stress state in an unbiased sample turned out to be tensile accompanied by a dominating $(00.\ell)$ texture component, the biased samples were found to exhibit an overall compressive stress and a $(h0.0)$ fiber texture. The results for the unbiased sample could be explained by a minimization of the elastic energy density which favors the preferred orientation of crystallographic *c* axes normal to the substrate plane. The biased samples closely resembled macroscopic Ti workpieces that were subjected to severe plastic deformation as was indicated by (i) the $(h0.0)$ fiber texture along the load direction, (ii) the large compressive in-plane residual stress $\sigma_\perp$, and (iii) the depth-resolved course of $\sigma_\perp(z)$. It is concluded that a high ion flux onto a growing Ti film has the same effect as a uniaxial mechanical load stress would have. © *2004 American Institute of Physics*.
[DOI: 10.1063/1.1814413]

## I. INTRODUCTION

Residual stress (RS) and preferred grain orientation (PO) represent important structural features of polycrystalline thin films that might significantly influence the intended functionality. Especially in hard nitride coatings for wear and abrasive protection, RS is a highly relevant issue.[1] An extreme case is represented by cubic boron nitride, c-BN, where the film delaminates from the substrate when a critical thickness of some hundred nanometers is exceeded.[2] Preferred orientation of crystallites or texture, on the other hand, is observed in practically all thin polycrystalline films grown by physical vapor deposition (PVD) techniques. Like residual stress, preferred orientation may significantly influence thin-film properties, which is not only known from nitride hard coatings[3–17] but also from semiconducting silicon thin films[18–26] and transparent-conductive ZnO:Al electrodes,[27–29] etc.

An important question is the interrelation between residual stress and preferred orientation in nitride hard coatings for which the effect of a concomitant change of both has been demonstrated.[6,8,14] These coatings were prepared in vacuum-based plasma-assisted processes, where use has been made of an ion bombardment of the growing film. The strength of the ion flux to the surface of the growing film was identified as one of the most relevant depositions parameters and its variation may drastically alter film structure and properties.[6,7,14] In order to observe the mentioned phenomena, high ion fluxes in excess of 1 $\mathrm{mA/cm^2}$ have to be realized or, to be more specific, the ratio of impinging ions over condensed atoms, abbreviated by $J_i/J_a$, must significantly exceed unity. This technical presupposition might be fulfilled, for instance, in the unbalanced magnetron sputter configuration or by pulsing the sputtering target.[26,30] Only recently, the introduction of midfrequency (MF) pulsing the substrate has been shown to enable ion fluxes of comparable strength and the preparation of thin films of so-far unobserved properties.[31,32]

In this work, we endeavor to elucidate the state of RS and PO in thin Ti films that are used as adhesion layers for hard coatings. Some 100-nm-thin Ti films were prepared by the gas-flow sputtering (GFS) technique in a regime of high ion bombardment. The GFS technique is based on the hollow cathode effect and has been developed as a high-deposition rate process in the last 1.5 decades.[32–38]

[a)]Present address: ihp-microelectronics, Im Technologiepark 25, D-15236 Frankfurt (Oder); electronic mail: birkholz@ihp-microelectronics.com

 

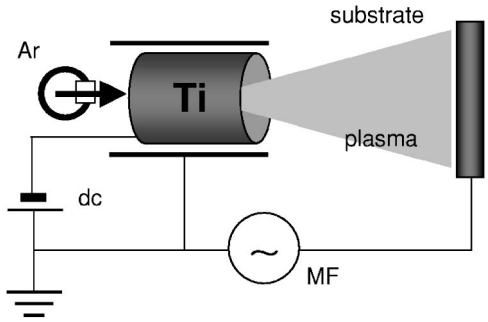


FIG. 1. Schematic deposition configuration of gas-flow sputtering experiments.

In spite of the seeming simplicity of a one-elemental material, the growth of thin Ti films was revealed in previous studies to represent a complex system. Magnetron-sputtered Ti coatings deposited at liquid-nitrogen temperatures were found to assume the high-temperature bcc or $\beta$ modification instead of the room-temperature stable hcp modification and to develop a ($hh0$) fiber texture.[39] Popeller and Abermann[40] have studied the growth stress of thin evaporated layers prepared under UHV conditions. The growth mode and stress state were revealed to be significantly influenced by the incorporation of residual oxygen and water from the gas phase and hydrogen from the substrate.[40]

The common investigation of both texture and RS was performed in this work by x-ray diffraction (XRD) procedures. Since the structural properties of thin films were demonstrated in a large body of work to sensitively depend on the film depth,[23,29,40,41] we chose the scattering vector technique for the investigation of RS. This method has recently been introduced into the field[42] and enables a depth-resolved evaluation of residual stresses on a length scale of the inverse x-ray attenuation coefficient.[43,44] We will present the results of a texture analysis and a depth-resolved residual stress analysis for a set of Ti samples deposited by GFS under various bias conditions. The PO and RS states in the prepared films will be compared with results on macroscopic Ti workpieces that were subjected to severe plastic deformation.

## II. SAMPLE PREPARATION AND ION BOMBARDMENT

The GFS process is schematically shown in Fig. 1. The total pressure is in the 10–100-Pa range, which has important consequences: (i) the mean free path of gas atoms and molecules is in the 100-$\mu$m range, i.e., (ii) neither gas atoms nor ions follow line-of-sight trajectories from the target to the substrate, but (iii) sputtered atoms are retarded to thermal energies within a few 10 mm.[37] In the investigations presented here, a cylindrical Ti tube ($\varnothing_i$40 mm $\times$ 60 mm) was utilized as target, while the pressure was set to 40 Pa by adjusting the Ar flow to 850 standard cubic centimeter per minute (SCCM).

Deposition experiments were carried out by applying a constant electrical power of 2.5 kW (ENI DCG-100 generator) onto the Ti target, equivalent to a power density of 33 W/cm$^2$. The discharge voltage amounted to values around 690 V, and the discharge current reached values of about 3.6 A. A planar metallic substrate holder with an active area of $A=100\times140$ mm$^2$ exposed to the plasma was positioned 107 mm in front of the target aperture. The substrate holder could be separately biased by a midfrequency generator, Advanced Energy Pinnacle Plus 5 kW. Polished shims of 100Cr6 steel (DIN 1.2067) were used as substrates ($\varnothing$35 mm $\times$ 3 mm). The process chamber was evacuated to a base pressure of some $10^{-2}$ Pa after introducing the substrates. Prior to the depositions, the substrate surfaces were cleaned by a plasma etching step, for which the total pressure amounted to 5 Pa (40 SCCM Ar). The Ti coatings were immediately deposited after the etching step within a deposition time of 300 s and at a rate $R$ of about 1 nm/s as estimated from the x-ray reflectometry (XRR) results.

Three different substrate bias modes were employed for the preparation of titanium coatings. For the first two samples, the generator was run in the constant-voltage mode to exert a nominal bias voltage, $V_B$, of −100 V with a frequency, $\nu$, of 100 kHz to the substrate holder and the substrate, which both were at the same electrical potential. The two experiments differed in the duration of the voltage pulse, $t_{on}$, that was varied by adjusting the delay time, $t_{off}$, to 0.5 and 5 $\mu$s, and which is equivalent to a duty cycle, $\nu\cdot t_{on}$, of 95% and 50% (RQTi1 and RQTi2). The third sample was deposited without a bias voltage leaving the substrate holder in a floating electrical state associated with a self-biased substrate (RQTi3). The different substrate bias parameters are listed in Table I.

The substrates were not intentionally heated during the process. However, a certain temperature increase could be observed in preliminary experiments, in which an electrically isolated temperature element was clamped to the back of the substrate. In order to deal with the thermal inertness of the substrate and the substrate holder, the actual temperature at the surface of the growing film was assumed to be accounted for by the saturation value, the temperature transient attained after some minutes of running the process. According to this procedure, the deposition temperature $T_d$ was estimated to be about 420 K in the unbiased experiment and about 460 K in the biased depositions. The homologous temperature, $T_h = T_d/T_m$, of the process was thus in the 0.22–0.24 range,

TABLE I. Midfrequency substrate bias parameters during preparation of Ti layers and derived quantities.

| RQTi No. | $U_B$ (V) | $\nu$ (kHz) | $t_{off}$ ($\mu$s) | $I_B$ (mA) | $I_B$/A (mA/cm$^2$) | $J_i$ $10^{15}$ Ar$^+$/(cm$^2$s) |
|---|---|---|---|---|---|---|
| 1 | −100 | 100 | 0.5 | 320–330 | 2.3 | 15 |
| 2 | −100 | 100 | 5 | 910–940 | 6.5 | 41 |
| 3 | 0 | 0 | 0 | | Floating | |

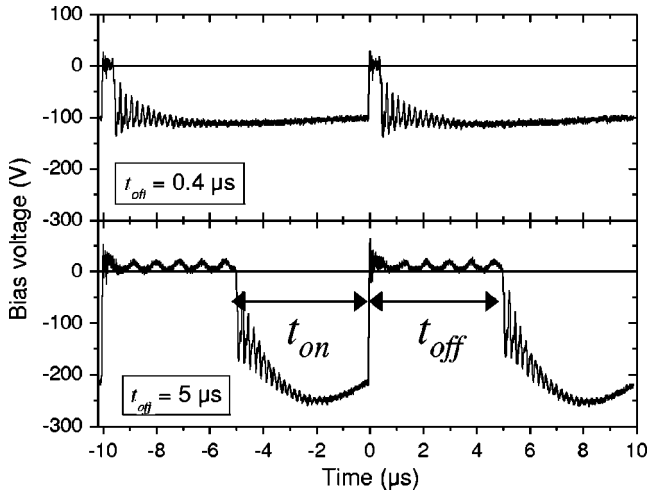


FIG. 2. Voltage transients of MF bias potential at the substrate holder measured parallel to the plasma. For all measurements, the adjusted midfrequency and the magnitude of the pulse-on voltage amounted to 100 kHz and −100 V, while the delay time or pulse-off time was varied from 0.4 (top) to 5 $\mu$s (bottom).

when the melting temperature of titanium, $T_m = 1927$ K, is inserted. Heating effects have already been observed in other MF-assisted processes. Kelly *et al.* attributed the effect mainly to the large electron current drawn to the substrate holder during the pulse delay time, when a small positive voltage is applied.[31]

Evidently, the heating effect might be reduced by minimizing the interaction of the plasma with the sample, but no such measures were taken in the experiments reported here. One of the few Langmuir probe studies of the GFS process evaluated the plasma density, $N_i$, for a parallel-plate configuration.[45] $N_i$ was found in the range of $3-5 \times 10^{18}$ m$^{-3}$ for power densities of a few W/cm$^2$ and distances from the target edge of some centimeters. From these data and the increased power density in the experiments presented here, we estimate the plasma density in the deposition process to be on the order of some $10^{19}$ m$^{-3}$.

In order to gain more insight into the ion bombardment associated with the MF biasing, we measured the voltage transients (Tektronix TDS 3032) to which the substrate holder was subjected. These experiments were performed under the same conditions as given above except for the dc target power which was set to 1 kW. Two voltage transients are shown in Fig. 2. They were both measured for the constant-voltage mode of the generator with a nominal pulse voltage of −100 V at a cycle frequency $\nu$ of 100 kHz. The different curves display the transients for delay times $t_{\mathrm{off}}$ of 0.4 and 5 $\mu$s. The positive counterpulse, preceding the negative pulse, is clearly recognized to have an average amplitude of some percent of the main pulse amplitude for $t_{\mathrm{off}} = 5$ $\mu$s. Moreover, the negative pulse is realized to amount to much larger values than the nominal −100 V that were adjusted at the generator. The effect of overshooting was observed to increase with increasing delay time, only for $t_{\mathrm{off}} = 0.4$ $\mu$s the pulse voltage is roughly equal to the intended value, while for $t_{\mathrm{off}} = 5$ $\mu$s it is—on the average—larger by about 100%. The voltage transients obtained for $t_{\mathrm{off}} = 0.4$ $\mu$s in these preliminary experiments compared well with those obtained for $t_{\mathrm{off}} = 0.5$ $\mu$s as applied for the preparation of sample 1.

The associated ion bombardment under these process conditions could be estimated from the bias current, $I_B$, as was indicated on the display of the generator. According to the manufacturer, this value can be considered as an approximate measure of the ion current drawn to the substrate during the pulse-on period.[31] In fact, this assumption will hold if all electrons are repelled from the substrate, i.e., if the bias voltage is of the order of −100 V or higher. This was in fact the case for most of the time during the pulse-on period, see Fig. 2. The ion current density $I_B/A$ and ion flux $J_i$ in units of elementary charges per unit time and unit face were derived from $I_B$ by dividing with the surface of the substrate holder $A$, see Table I. The current density is seen to take large values of 2.3 and 6.5 mA/cm$^2$ which are otherwise obtained in PVD techniques only by virtue of special magnetic-field configurations[6,7,14] or by pulsing the target.[30] It has to be emphasized that the obtained $J_i$ values are only rough estimates, since, for instance, the effect of secondary electron emission has been neglected. It may be concluded, however, that the GFS process in combination with a MF-biased substrate enables plasma-assisted depositions with a large ion flux to the surface of the growing film.

## III. X-RAY DIFFRACTION AND REFLECTOMETRY IN SYMMETRIC $\theta/2\theta$ CONFIGURATION

The prepared samples were first investigated in symmetric $\theta/2\theta$ geometry with a Panalytical material research diffractometer that was operated with a Cu anode at 40 kV and 40 mA. A fast-counting multiple stripe detector (X'Celerator) was used in the high resolution, step scan mode (0.01°/2.1 s). The measured diffractograms are displayed in Fig. 3, where also the pattern of the uncoated 100Cr6 shim is shown. The ferrite (110) reflection is clearly recognized in all patterns at $2\theta_0 = 44.6°$. The asymmetry of the peak is due to the overlapping with the austenite (111) on the small-angle side, $2\theta_0 = 43.5°$. Reflex positions according to the International Center for Diffraction Data (ICDD) cards of ferrite and austenite are shown in the plot. Next to the substrate peaks, the Bragg reflexes of the hcp Ti phase are clearly recognized ($c/a = 1.587$). The relative intensities of (10.0), (00.2), and (10.1) reflections differ strongly for the three samples. For the unbiased sample 3, the (00.2) reflection is the strongest, indicating a preferred orientation of grains with their $c$ axis in direction of the substrate normal $\boldsymbol{n}_{sub}$. For the biased samples 1 and 2, the texture changes to ($h$0.0).

The thickness and density of Ti layers were evaluated by XRR in the scattering angle range $0 \leqslant 2\theta \leqslant 4°$. For this purpose, the same Panalytical diffractometer was employed, but in these experiments, the divergent x-ray bundle was converted to a quasiparallel beam by a multilayer mirror and scattered intensities were measured by a scintillation counter. It turned out that the measured reflection curves could accurately be simulated when a $TiO_x$ layer of a few nanometers thickness was assumed on top of the Ti layer. The $TiO_x$ layer

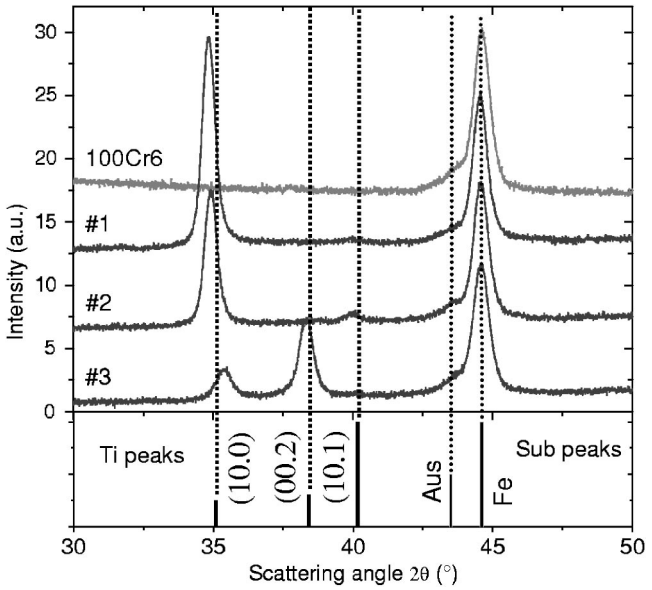


FIG. 3. X-ray diffraction pattern of the three Ti layers 1–3 prepared on steel substrates and of an uncoated 100Cr6 substrate (Sub, on top). The bars give the position and relative intensities of Bragg peaks of the individual phase according to ICDD database (Ti=hcp titanium, Aus=austenite, and Fe =ferrite).

indicates a postoxidation of the Ti surface, and such oxidation processes were identified in numerous XRR studies on thin metal layers. The results of the simulations are presented in Table II. As could have been expected, the two biased samples 1 and 2 are more compact than the unbiased sample 3. Also, the thickness of the latter deviates significantly from the two other samples as does the surface roughness. Summarizing, it can be stated that the structural properties measured by XRR differ only a little for samples 1 and 2. They are distinct, however, from the unbiased sample 3, which does not have the high degree of compactness, but is thicker and exhibits a more pronounced surface roughness.

The quantity $J_a$ given in Table II stands for the number of built-in Ti atoms as derived from the XRR-determined thickness and density. The ratio of impinging ions $J_i$ over $J_a$ is the decisive parameter in characterizing the amount of ion bombardment during film growth. In experiments 1 and 2, $J_i/J_a$ is seen to become 2.7 and 7, respectively, being significantly larger than 1.

## IV. DETERMINATION OF TEXTURE BY X-RAY DIFFRACTION

Texture as well as residual stress analysis were performed with Co $K\alpha$ radiation at 32 kV and 50 mA (Co $K\alpha$ =179 pm) on a new type of five circle diffractometer ("ETA-diffractometer"), which has been developed in a cooperation between SEIFERT and the Hahn-Meitner-Institute. Compared with a conventional four circle diffractometer (Eulerian cradle), it is equipped with an additional axis $\Phi_1$ which permits a direct rotation of the sample around the diffraction vector, $\boldsymbol{g}_{hkl}$, for any orientation with respect to the sample reference system.[46]

Intensity pole figures obtained for the reflections $(hk.\ell)=(10.0)$, (00.2), and (10.1) are displayed in Fig. 4. The pole figures were measured conventionally by varying the azimuth $\phi$ and tilt angle $\psi$ and measuring the integral intensities. Maximum and minimum intensities are given in each single plot. Pole figures were corrected for both background and layer thickness using the program MULTEX®.[47] The results indicate a preferred crystallite orientation in the form of strong fiber textures for all samples. However, significant differences are found between layers 1 and 2 on the one hand and the unbiased layer 3 on the other hand. In the first case, the $\langle 10.0\rangle$ pole at $\sim 0°$ and the distinct ring-shaped $\langle 10.1\rangle$ poles observed at $\sim 29°$ ($\langle 10.1\rangle$) and $\sim 64°$ ($\langle 01.1\rangle$), respectively, reveal a $\langle h0.0\rangle$ fiber texture. The fiber is stronger for layer 1 than 2, exhibiting maximum intensities of 11.3 and 7.7. In the case of layer 3, comparable intensities are observed for the (10.0) and (00.2) reflections at the origin. A thorough analysis by means of the inverse pole figure technique revealed the MF-biased samples 1 and 2 to exhibit pronounced $(h0.0)$ fiber textures, whereas the preferred orientation in the unbiased sample 3 is dominated by a $\langle 00.\ell\rangle$ fiber.

The uniaxial rotational symmetry of textures is in accordance with the deposition geometry, see Fig. 1. Axial symmetric textures or fiber textures are typically observed in thin films when no special direction is emphasized by the process geometry. In such cases, the stress field can be expected to be axially symmetric, too, and is fully accounted for by a single component, $\sigma_{\|}$, for the in-plane stress.

## V. RESIDUAL STRESS ANALYSIS

### A. Conventional sin² ψ method

In order to gain comprehensive information on the layer-inherent residual stress state, different methods of x-ray stress analysis (XSA) were applied. For the parallel beam setups, a polycapillary semilens in the primary beam and a grazing incidence x-ray diffraction unit consisting of a 0.4° Soller slit and a (001) LiF monochromator in the diffracted beam were used in order to reduce the Ti fluorescence radiation and to prevent the geometrical diffraction line broadening.

TABLE II. XRR-determined structural parameters of Ti layers and derived quantities $J_a$ and $J_i/J_a$.

| RQTi No. | $t$ (nm) | $R$ (nm/s) | $\rho$ (g/cm$^3$) | $\rho/\rho_{h\text{-Ti}}$ (%) | Roughness (nm) | $J_a$ ($10^{15}$/cm$^2$s) | $J_i/J_a$ |
|---|---|---|---|---|---|---|---|
| 1 | 296 | 0.99 | 4.496 | 99.7 | 4.8 | 5.57 | 2.7 |
| 2 | 313 | 1.04 | 4.473 | 99.2 | 4.4 | 5.86 | 7.0 |
| 3 | 409 | 1.36 | 4.468 | 99.1 | 7.4 | 7.66 | ./. |

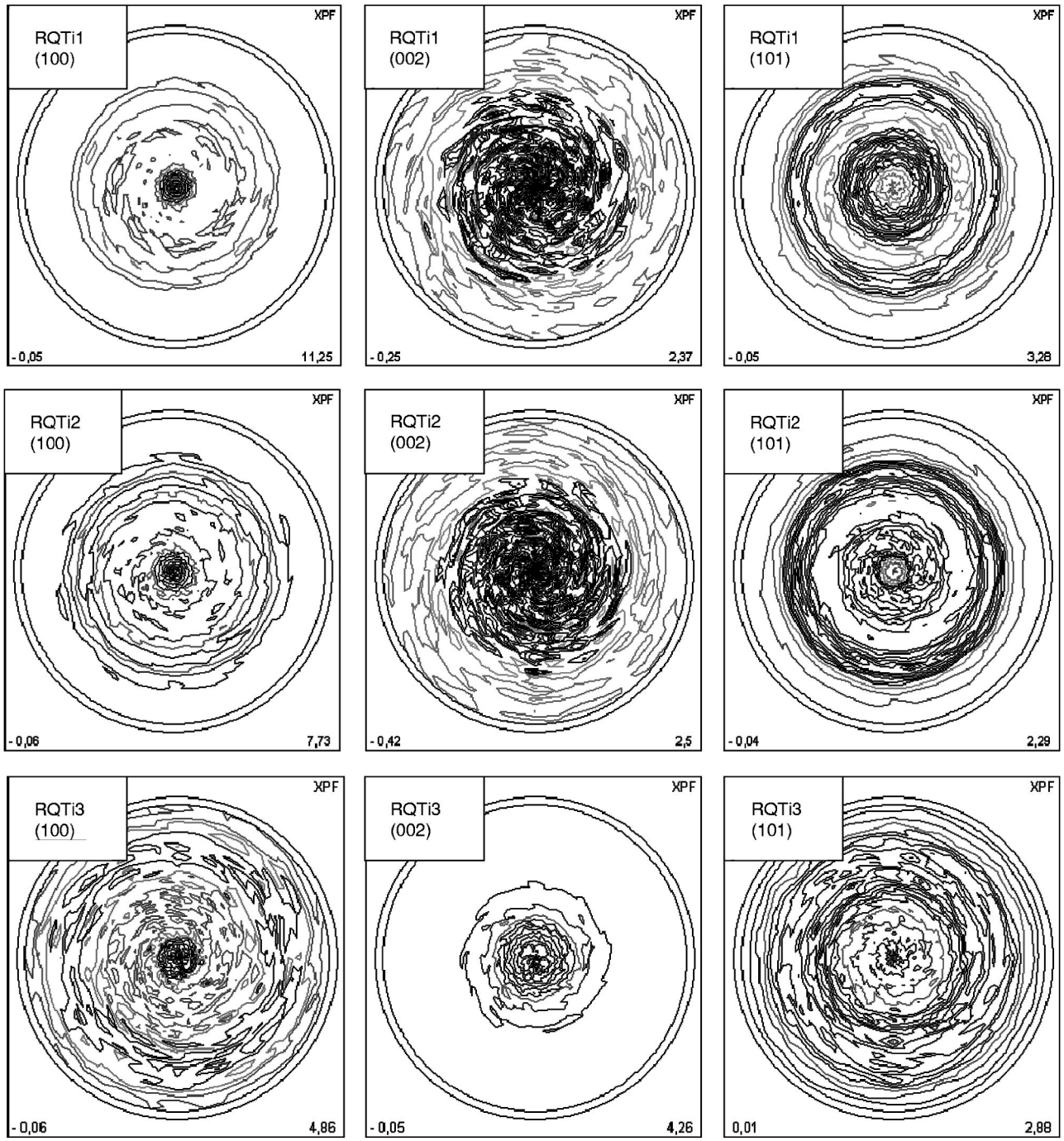


FIG. 4. Intensity pole figures of the three Ti layers obtained for the three strongest reflections (10.0), (00.2), and (10.1). Minimum and maximum values of the intensity distributions are given at the bottom of each figure.

In the first step, we applied the conventional $\sin^2\psi$ method,[48] which yields an average value, $\langle\sigma_\parallel\rangle$, of the in-plane film stress from the slope of the $d(hkl)$ versus $\sin^2\psi$ plots obtained by stepwise tilting the sample around an axis parallel to the diffraction plane ($\Psi$ mode). Despite the strong texture, sufficient intensity was diffracted at the (10.0) and at the (10.1) lattice planes, respectively, within a wide range of $\sin^2\psi$. Figure 5 gives the $d(hkl)$ versus $\sin^2\psi$ distributions for the (10.1) reflections of the three samples. We found almost linear $d$ versus $\sin^2\psi$ distributions with a clear negative slope, indicating compressive in-plane stresses in both ion-bombarded layers 1 and 2, whereas the positive slope observed for layer 3 reveals the presence of tensile stresses within the film. The small oscillations of the data are probably due to the texture, i.e., the effect of macroscopic elastic anisotropy on the macroscopic scale,[49] rather than to residual stress gradients.

We used the model of Eshelby and Kröner[50,51] to calculate the diffraction elastic constants, $s_1(hkl)$ and $\frac{1}{2}s_2(hkl)$, needed for stress evaluation from the single-crystal elastic constants, $c_{ij}$, of titanium, see Table III.[52] The results of the $\sin^2\psi$ analysis are summarized in Table IV. Comparing the average in-plane residual stresses, $\langle\sigma_\parallel\rangle^{100}$ and $\langle\sigma_\parallel\rangle^{101}$, ob-

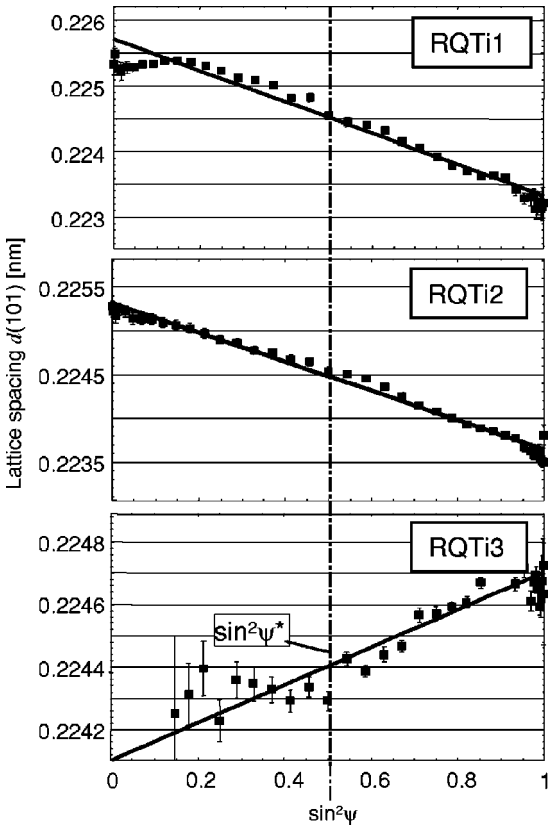


FIG. 5. $d$ vs $\sin^2\psi$ plots, Co $K\alpha$, (10.1) reflection. The solid lines correspond to the Reuss straight line, the slope of which yields the average in-plane layer stress $\langle\sigma_{\parallel}\rangle$. $\sin^2\psi^*$ marks the position that corresponds to the strain-free direction of the biaxial stress state.

tained for the two investigated reflections (10.0) and (10.1), respectively, we found a very good agreement for the samples 1 and 2, but a large difference between the individual values for Ti film 3. We exclude experimental artifacts to be the reason for this unusual behavior, but assume that the complex texture in combination with second kind microstresses, $\langle\sigma^{II}\rangle$, is responsible for the seemingly contradicting results of sample 3.

### B. The scattering vector method

In the second step, the scattering vector method was applied, which has been developed especially for x-ray stress gradient analysis in strongly textured thin films.[42,43,46] As in the conventional $\sin^2\psi$, method, the shift of the Bragg angle $\theta$ is measured for different orientations of the sample. But in contrast to the $\sin^2\psi$-based methods of the XSA, lattice spacing depth profiling is performed by recording the diffraction profiles after the stepwise rotation of the sample around the diffraction vector, $\boldsymbol{g}_{hkl}$, named "$\eta$-scan." This rotation by

TABLE III. Diffraction elastic constants for the different evaluated reflections calculated by means of the Eshelby-Kröner model.

| $hk.l$ | $s_1(hkl)$ ($\times 10^{-6}$ MPa$^{-1}$) | $\frac{1}{2}s_2(hkl)$ ($\times 10^{-6}$ MPa$^{-1}$) |
|---|---|---|
| 10.0 | −2.98 | 12.03 |
| 10.1 | −2.90 | 11.80 |

angle $\eta$ changes the diffraction geometry continuously from the $\Psi$ mode into the $\Omega$ mode of the XSA and concomitantly varies the penetration depth $\tau$[49] which is generally defined[42] by

$$\tau = \frac{\sin^2\theta - \sin^2\psi + \cos^2\theta\sin^2\psi\sin^2\eta}{2\mu\sin\theta\cos\psi} \tag{1}$$

with $\mu$ accounting for the linear attenuation coefficient of Ti being 0.1326 $\mu$m$^{-1}$ for Co $K\alpha$. Thus, $\tau$ can be varied even for fixed orientations $\psi$ of $\boldsymbol{g}_{hkl}$, enabling a straightforward evaluation of the residual stress profiles from the measured strain profiles. For a biaxial residual stress state of rotational in-plane symmetry (i.e., $\sigma_{11}=\sigma_{22}=\sigma_{\parallel}$), the fundamental equation of the XSA yields

$$\sigma_{\parallel}(\tau) = \frac{\varepsilon_{\psi}(hkl,\tau)}{\frac{1}{2}s_2(hkl)\sin^2\psi + 2s_1(hkl)} \tag{2}$$

with $\varepsilon_{\psi}(hkl)=\{d_{\psi}(hkl)-d_0(hkl)\}/d_0(hkl)$ and $d_0(hkl)$ giving the strain-free lattice parameter. Because of the exponential attenuation of x rays in matter, the experimentally obtained strain depth profiles as well as the stress profiles derived from Eq. (5) are the exponentially averaged "Laplace profiles" of the corresponding $z$-space profiles, $\varepsilon_{\psi}(hkl,z)$ and $\sigma_{\parallel}(z)$, respectively,

$$\varepsilon_{\psi}(hkl,\tau) = \int_0^t \varepsilon_{\psi}(hkl,z)e^{-z/\tau}dz \Big/ \int_0^t e^{-z/\tau}dz, \tag{3}$$

$$\sigma_{\parallel}(\tau) = \int_0^t \sigma_{\parallel}(z)e^{-z/\tau}dz \Big/ \int_0^t e^{-z/\tau}dz, \tag{4}$$

with the layer thickness, $t$, as the upper integration limit. Here, we chose to elucidate the variation of (10.1) reflections. For samples 1 and 2 we performed lattice spacing depth profiling in the scattering vector mode at $\psi=29°$ and 64°, respectively, which corresponds to the $\langle 11.0\rangle$ texture poles, and at $\psi=55°$, 65°, and 75° for layer 3. The appropriate tilt angles, $\psi$, were chosen from the inspection of (10.1) pole figures, compare Fig. 4, by selecting angles from large intensity regions to improve the statistical significance of measured data. For the evaluation of the in-plane stress depth profiles, we applied a variation procedure, which is based on the high sensitivity of the lattice strain, $\varepsilon(hkl)$, with respect to $d_0(hkl)$. So it becomes obvious that two or more stress depth profiles, $\sigma_{\parallel}^{(\psi_i)}(\tau)$, obtained according to Eq. (5) for different inclinations, $\psi_i$, will only fit together in the sense of a "universal plot," if the correct $d_0(hkl)$ is used. This criterion, however, can be used to determine $d_0(hkl)$ itself.[42,46]

The results obtained by means of the scattering vector method are summarized in Fig. 6. The real-space stress distribution in the layers was approximated by a linear model $\sigma_{\parallel}(z)=c_0+c_1 z$, for which the corresponding Laplace transform was calculated from Eq. (7)

$$\sigma_{\parallel}(\tau) = c_0 + c_1\left(\tau - \frac{te^{-t/\tau}}{1-e^{-t/\tau}}\right) \tag{5}$$

and fitted to the discrete stress data. In all cases, the residual stress state was found to be nonuniform with respect to the

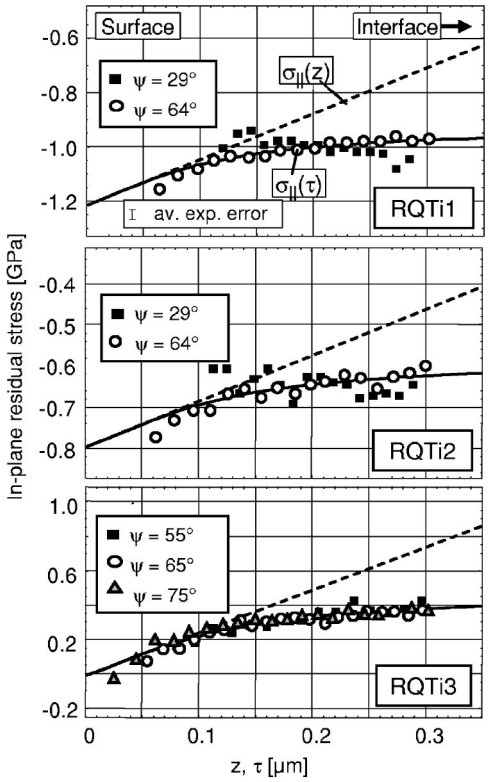


FIG. 6. In-plane residual stress profiles evaluated by means of the scattering vector method. The straight lines give the fit to measured data points, while the dashed lines indicate their inverse Laplace transform to yield the real-space depth distribution $\sigma_{\parallel}(z)$. The films' surfaces are at $z=0$.

layer thickness. So we observed a decrease of the compressive stresses towards the interface between the layer and the substrate for samples 1 and 2. The shift goes in the same direction for layer 3, but the stresses are tensile on an absolute scale. Furthermore, the average stresses $\langle\sigma_{\parallel}\rangle$ obtained by means of the $\sin^2\psi$ method (cf. Table IV) fit quite well into the depth profiles.

However, this argument applies for the unbiased layer 3 only for the (10.1) reflection. For this reason, we performed additional measurements in the scattering vector mode at the (10.0) reflection, and found a quite similar stress depth profile like that shown at the bottom of Fig. 5, but shifted by about 500 MPa towards higher tensile stresses (not shown here). On the one hand, the $\sin^2\psi$ method and the scattering vector method are concluded to yield comparable results for each of the investigated reflections (10.0) and (10.1), although they differ by about 500–600 MPa on the absolute scale on the other hand. As mentioned before, we assume that both the rather complicated texture of this layer and the second kind of microstresses $\langle\sigma^{II}\rangle$ could be responsible for these findings. Further research work will be necessary to give evidence for this hypothesis.

TABLE IV. Results of the residual stress analysis based on the $\sin^2\psi$ method.

| RQTi No. | $\langle\sigma_{\parallel}\rangle^{100}$ (MPa) | $\langle\sigma_{\parallel}\rangle^{101}$ (MPa) |
|---|---|---|
| 1 | −1059±38 | −900±25 |
| 2 | −614±14 | −632±11 |
| 3 | 787±37 | 227±18 |

TABLE V. (*10.1*) lattice spacings measured in the strain-free direction $\psi^*$ of the biaxial residual stress state and obtained by means of a variation procedure for $d_0$ and residual stress gradient evaluation in the frame of the scattering vector method (Ref. 43), respectively.

| RQTi No. | $d_{\psi^*}(10.1)$ (nm) | $d_0^{SVM}(10.1)$ (nm) |
|---|---|---|
| 1 | 0.22454 | 0.22456 |
| 2 | 0.22449 | 0.22448 |
| 3 | 0.22440 | 0.22425 |

In order to exclude systematic deviations from the biaxial stress model due to residual stress fields $\sigma_{33}$ normal to the film plane, we compared the lattice spacings, $d_{\psi^*}(101)$, measured in the strain-free direction $\psi^*(hkl) = \arcsin\sqrt{-2s_1(hkl)/1/2s_2(hkl)}$ of a pure biaxial stress state with the lattice spacings $d_0^{SVM}(101)$ obtained for the strain-free lattice spacing $d_0(101)$ within the framework of the scattering vector method (Table V). Deviations of $d_{\psi^*}(hkl)$ from the strain-free lattice spacing $d_0(hkl)$ are correlated with $\sigma_{33}$ by

$$\sigma_{33} = \frac{d_{\psi^*}(hkl) - d_0(hkl)}{d_0(hkl)\left[\frac{1}{2}s_2(hkl) + 3s_1(hkl)\right]}, \tag{6}$$

which can be used at least for an estimation of the normal stress.[42] Inserting the respective lattice spacings summarized in Table V into Eq. (9) yielded only very small values for $\sigma_{33}$ of some 10 MPa, and therefore, we conclude a nearly perfect biaxial stress state within all three layers.

## VI. DISCUSSION

According to the structure zone model (SZM),[41,53–55] the samples prepared at a homologous temperature of 0.22–0.24 would have to be categorized into zone 1*bT* into the notion of Machlin, where growth is determined by (i) medium adatom mobility and (ii) medium grain-boundary migration.[41] It should be remembered that (i) is only operative for the topmost atomic layer, while (ii) is active after burying the grains by subsequent deposition and might even operate after stopping the deposition process, compare Ref. 40. For structure zone 1*bT*, important examples from the group of metallic materials were reported in the literature, where the morphology, texture, and RS were shown to be determined by grain-boundary migration, i.e., secondary recrystallization, the driving force stemming either from the energy of crystallite fusion or from the relaxation of built-in stress.

It should be noted that the categorization of the Ti depositions performed in this work into the SZM has to account for the high ion bombardment. The impact of hyperthermal particles on the growing film is generally considered to be associated with an increase in adatom mobility and an acceleration of grain-boundary migration.[41] The ion bombardment will thus lead to a shift of film morphology into a structure zone of a higher, effective homologous temperature, $T_{\mathrm{hom,eff}} > T_{\mathrm{hom}}$. The effect may especially be pronounced in

experiments with MF biasing the substrate due to the heating by incoming electrons reaching the film during pulse delay time.

Regarding the effect and the nature of the ion flux, an interesting conclusion can be drawn from a comparison of deposition rates $R$. It is seen from Table II that $R$ remains almost unchanged for samples 1 and 2 but increases for the unbiased sample 3. The first values are about 25% smaller than the latter. We assign this material lack to a resputtering effect that occurred due to the impacting $Ar^+$ ions during the pulse-on period. It is evident from the sputter yield curve $Y(E)$ of Ti in the low-energy range[56] that the average ion energy $E_i$ will lie above the threshold value to cause a displacement of atoms in the Ti lattice-like generation of interstitials. The value for the latter amounts to about 3 eV in metals,[57] and from the 25% resputtering and inspection of the $Y(E)$ curve it can safely be assumed that the majority of impinging $Ar^+$ surmounted this value. It is thus derived that the kinetic energy $E_i$ of the majority of impinging ions is below the threshold to cause a complete resputtering of the layer but is larger than the lattice displacement energy, $E_{dis} < E_i < E_{sp}$.

The most significant point with respect to the average stress in all three samples is the change from a tensile stress in sample 3 to a compressive RS in samples 1 and 2 by the usage of MF biasing the substrate. This is in agreement with the stress reversal observed in magnetron-sputtered metal films[58] which may be switched from tensile to compressive by bombarding the surface with a large ion flux. The residual stress in thin films that are not subjected to a large ion flux is mostly found to be tensile, which is understood in the grain-boundary relaxation model to be caused by the coalescence of neighboring growth columns associated with an extension of interatomic bonds in the film plane.[58,59] The transition to a compressive stress by biasing the substrate could be modeled in sputter deposition processes by a forward sputtering mechanism based on knock-on linear cascade theory. A tensile-compressive threshold was identified from experiments to scale with the ion flux $J_i$. It was argued that the threshold would be given by the atomic displacement energy of metal atoms in the deposited crystallographic structure.

This approach was found to explain a large set of experimental observations although uncertainties remained with respect to the nature of compressing species and the question of the underlying mechanism (energy or momentum controlled).[58] From the RS measurements of our samples, we conclude that a comparable stress reversal may be initiated in gas-flow sputtering by MF biasing the substrate and dragging a large ion flux to the metal film. This finding could not have been simply expected since neutrals and ions in the GFS process suffer a much higher collision rate in the gas phase than in MS processes.

The elastic energy density stored in both the unbiased and MF-biased films can be estimated on the basis of a simple assumption. The elastic energy density depends for coinciding sample coordinate and crystallographic coordinate system $(x^S_i \| x^C_i)$ according to

$$\overline{V} = \tfrac{1}{2}(s_{1111} + s_{2222} + 2s_{1122})\sigma_{\|}^2 \tag{7}$$

on the in-plane residual stress $\sigma_{\|}$ and the elastic compliances $s_{ijkl}$ of the monocrystal. If the samples are assumed to exhibit a perfect $(00.\ell)$ texture and Ti data [$s_{1111}=s_{2222}=9.59$, $s_{3333}=6.99$, $s_{1122}=-4.62$, and $s_{1133}=-1.90\times10^{-6}$ MPa (Ref. 52)] are inserted, this formula might directly be applied to yield an elastic energy density of

$$\overline{V}_{(00.2)} = (s_{1111} + s_{1122})\sigma_{\|}^2 = 4.97 \times 10^{-6}\ \mathrm{MPa}^{-1}\sigma_{\|}^2 \tag{8}$$

for a $c$-axis fiber texture. In case of a perfect $(h0.0)$ texture, the fourth-rank tensor $s_{ijkl}$ has to be transformed by the orthogonal matrix, $a_{13}=a_{22}=1$, $a_{31}=-1$, all other $a_{ij}=0$, into the sample-related coordinate system, $s_{ijkl} = a_{im}a_{jn}a_{ko}a_{lp}\, s_{mnop}$ (summation convention), and we obtain

$$\overline{V}_{(10.0)} = \tfrac{1}{2}(s_{1111} + s_{3333} + 2s_{1133})\sigma_{\|}^2 = 6.39 \times 10^{-6}\ \mathrm{MPa}^{-1}\sigma_{\|}^2 \tag{9}$$

for this texture type. Although these formulas would only apply on fully textured films, while the Ti samples exhibited further texture components, we may draw two tentative conclusions from them. Firstly, the $(00.\ell)$ fiber texture is realized to be energetically favored over a $(h0.0)$ fiber texture for a constant in-plane stress. It might thus be understood that a $(00.\ell)$ fiber developed in the case of sample 3, where the residual stress was argued to stem from the grain-boundary relaxation. However, the elastic energy is independent of the sign of $\sigma_{\|}$ and also the large compressive stresses in samples 1 and 2 would favorably accommodate to a $(00.\ell)$ texture. Since this is not the case, it is realized, secondly, that samples 1 and 2 occupy a metastable state regarding the stored elastic energy. The energy input that is necessary to excite the system to the higher-energy state would evidently have to be supplied by the large ion flux.

It is intriguing to compare the texture and the stress state with those of plastically deformed Ti or other close-packed structures as known from the investigations of bulk metals. The process of plastic deformation in metals is associated with a redistribution of grain orientations. Pronounced fiber textures typically evolve under uniaxial compression or uniaxial extension where those lattice planes are oriented parallel to the deformation direction that exhibit a low activation energy for deformational slip. In one-elemental metals, the preferred slip system $\{hk\ell\}\langle uvw\rangle$ is given in most cases by highly dense occupied lattice planes $\{hk\ell\}$. Plastic deformation is accompanied by a redistribution of orientations and might be monitored by $(hk\ell)$ and $(uvw)$ pole figures.

In hcp metals, the main active deformation mode might either be due to basal slip $\{00.1\}\langle 10.0\rangle$, prismatic slip $\{10.0\}\langle 00.1\rangle$, or pyramidal slip along $\{10.1\}$ lattice planes.[60,61] In principle, hexagonal metals are particularly sensitive to deformation by twinning, but it turned out that slip is generally favored over twinning in Ti leading to a substantial reduction of twinning at high strain.[62] In addition, prismatic slip $\{10.0\}\langle 00.1\rangle$ was identified as the main active deformation mode[61] and uniaxially deformed hcp Ti workpieces were found to exhibit pronounced axially symmetric

($h$0.0) deformation textures.[61,63] This is exactly the state of texture we observe for Ti films prepared under a high ion bombardment. Whereas strong intensity maxima are observed in (10.0) pole figures of samples 1 and 2, much less reflection intensity is collected in the origin of (00.2) pole figures; see the two topmost rows in Fig. 4. We conclude that the state of texture in the samples prepared under a high ion bombardment compares with a deformation texture as typically obtained for Ti bulk samples after severe plastic deformation.

We also have to point to the distinction between load stress (LS) and RS. In the deposition experiment, which we consider as a process of plasma loading, the stress tensor only had one compressional component in direction of the substrate normal, $\sigma^{LS}{}_{\perp} < 0$. If a macroscopic workpiece would be subjected to such a mechanical load, one would expect to measure residual stresses of tensile character along the deformation direction $\sigma^{RS}{}_{\perp} > 0$ and a compressed component in the transverse direction $\sigma^{RS}{}_{\parallel} < 0$. In addition, because of the equilibrium conditions the stress tensor has to obey, the RS component in the deformation direction will practically vanish in the vicinity of the surface, $\sigma^{RS}{}_{\perp} \approx 0$, while the transverse component would remain—albeit, exhibiting a reversed sign compared to loading. The sign conversion of stresses measured by diffraction techniques from the loading to the postloading state is an experimentally well-established fact, for which stresses of the second and third kind are considered as the main reason.[49] The residual stress outlined above is exactly the stress tensor that is observed by the XRD analysis of Ti films 1 and 2. We conclude that the RS tensor measured for MF-biased films is a further indication that these samples were subjected to plastic deformation by an out-of-plane compressive load during deposition.

A third indication for this hypothesis is given by the depth dependency of the in-plane RS component, $\sigma_{\parallel}(z)$. In the two biased samples, the compressive stress is realized to increase to its maximum value by approaching the surface from the interior, see Figs. 6(a) and 6(b). This can be compared with stress profiles as measured in macroscopic workpieces that were subjected to a shot peening treatment. In general, in these samples, the transverse residual stress is found to be compressive, too, and to increase to maximum values in the vicinity close to the surface.[49] It should be emphasized, however, that there exist some distinctions between the two stress states like a pronounced maximum in $\sigma_{\parallel}(z)$ that occurs in shot-peened material. We currently understand these distinctions by the different nature of the peening process that is performed in one case by atomic ions and in the other case by voluminous metallic or ceramic balls having diameters in the micrometer range. The two treatments are also clearly different by their dynamics, since in the atomic peening process the material is grown layer-by-layer while subjected to plasma loading.

To summarize, the state of preferred orientation and residual stress in Ti films prepared by MF biasing the substrate shows strong similarities when compared with macroscopic workpieces that were subjected to severe plastic deformation. From a comparison with a film prepared under free-floating conditions, it can be concluded that the observed changes in the thin-film structure are caused by the large ion flux onto the surface of the growing film.

## VII. CONCLUSIONS

The gas-flow sputtering technique was successfully applied to prepare thin Ti films under a high ion bombardment regime. This was achieved by MF biasing the substrate, which is associated with high ion fluxes in the $10^{16}$ $Ar^+/cm^2s$ range and a high ion-to-deposited-atom arrival ratio $J_i/J_a$. Two samples prepared under distinct high ion flux conditions and a third sample, prepared without ion bombardment under free-floating conditions, were structurally characterized by x-ray scattering techniques. X-ray stress analysis was carried out in the framework of the recently introduced scattering vector technique, enabling a depth-resolved determination of the RS state. Stress fields in all films were found to be fully accounted for by the biaxial stress model. The scattering vector technique yielded consistent results when compared with the conventional $\sin^2\psi$ technique, and the investigation has thus extended the proven range of usefulness for this technique. In-plane stresses, $\sigma_{\parallel}$, were found to decrease towards the film surface having their highest, i.e., most compressive values within the surface plane. Large compressive stresses between 0.6 and 1.2 GPa and a uniaxial texture with preferred $a$-axis orientation were observed for the samples prepared under high ion bombardment, whereas a tensile stress of about 0.2 GPa and a dominating $c$-axis fiber texture were identified in the unbiased sample.

The results on preferred grain orientation and residual stress in GFS-prepared Ti films were interpreted by a model of plasma loading; MF biasing the substrate causes a large flux of ions to be dragged to the substrate. During the deposition, every Ti atom of the topmost layer is on the average hit by more than one $Ar^+$ ion, $J_i/J_a > 1$. The ion energy surmounts the atomic displacement energy of the solid being deposited, but is lower than the sputter energy, $E_{\mathrm{dis}} < E_i < E_{\mathrm{sp}}$. Regarding the concomitantly obtained results on texture and residual stress, the MF-biased samples closely resemble plastic deformation, as known from studies on large-volume Ti workpieces. This is evidenced from the preferred orientation of preferential slip planes (00.1) along the load direction and the large compressive residual stress along the in-plane directions. It is argued that the ion flux from the plasma causes a rearrangement of deposited atoms in the topmost atomic layers. Because the process is active during growth, each layer is affected and a thin film is finally obtained, exhibiting a comparable microstructure as it would be induced in macroscopic material by mechanical loading. It is expected that the mechanism of "plasma loading," as outlined here for metallic Ti films, will also account for the state of residual stress and preferred orientation in other thin-film material systems.

[1] M. Ohring, *The Materials Science of Thin Films* (Academic Press, San Diego, 1992), Chaps. 9 and 12.
[2] W. J. Zhang, I. Bello, Lifshitz, and S. T. Lee, MRS Bull. **28**, 184 (2003).
[3] K. Helming and B. Rauschenbach, Phys. Status Solidi B **138**, K1 (1986).

[4]B. Rauschenbach and K. Helming, Nucl. Instrum. Methods Phys. Res. B **42**, 216 (1989).
[5]J. Pelleg, L. Z. Zevin, S. Lungo, and N. Croitoru, Thin Solid Films **197**, 117 (1991).
[6]F. Adibi, I. Petrov, J. E. Greene, L. Hultman, and J.-E. Sundgren, J. Appl. Phys. **73**, 8580 (1993).
[7]J. E. Greene, J.-E. Sundgren, L. Hultman, I. Petrov, and D. B. Bergstrom, Appl. Phys. Lett. **67**, 2928 (1995).
[8]A. Bendavid, P. J. Martin, X. Wang, M. Wittling, and T. J. Kinder, J. Vac. Sci. Technol. A **13**, 1658 (1995).
[9]M. Zeitler, J. W. Gerlach, T. Kraus, and B. Rauschenbach, Appl. Phys. Lett. **70**, 1254 (1997).
[10]C. Genzel and W. Reimers, Phys. Status Solidi A **166**, 751 (1998).
[11]A. Saerens, P. Van Houtte, B. Meert, and C. Quaeyhaegens, J. Appl. Crystallogr. **33**, 312 (2000).
[12]F. Engelmark, G. F. Iriarte, I. V. Katardijev, M. Ottoson, P. Muralt, and S. Berg, J. Vac. Sci. Technol. A **19**, 2664 (2001).
[13]F. H. Baumann *et al.*, MRS Bull. **26**, 182 (2001).
[14]C.-S. Shin, D. Gall, Y.-W. Kim, N. Hellgren, I. Petrov, and E. Greene, J. Appl. Phys. **92**, 5084 (2002).
[15]N. Schell, J. Bottiger, W. Matz, and J. Chevallier, Nucl. Instrum. Methods Phys. Res. B **199**, 133 (2003).
[16]J. Almer, U. Lienert, R. L. Peng, C. Schlauer, and M. Odén, J. Appl. Phys. **94**, 697 (2003).
[17]Y. Kajikawa, S. Noda, and H. Komiyama, J. Vac. Sci. Technol. A **21**, 1943 (2003).
[18]T. I. Kamins and T. R. Cass, Thin Solid Films **16**, 147 (1973).
[19]R. Bisaro, J. Maraino, N. Proust, and K. Zellama, J. Appl. Phys. **59**, 1167 (1986).
[20]H.-R. Wenk, M. Sintubin, J. Huang, G. C. Johnson, and R. T. Howe, J. Appl. Phys. **67**, 572 (1990).
[21]Y. Sun, T. Miyasato, and J. K. Wigmore, Appl. Phys. Lett. **70**, 508 (1997).
[22]K. Nakahata, A. Miida, T. Kamiy, Y. Maeda, C. M. Fortmann, and I. Shimizu, Jpn. J. Appl. Phys., Part 2 **37**, L1026 (1998).
[23]M. Birkholz, B. Selle, E. Conrad, K. Lips, and W. Fuhs, J. Appl. Phys. **88**, 4376 (2000).
[24]O. Nast, T. Puzzer, C. T. Chou, and M. Birkholz, in *16th European Photovoltaic Solar Energy Conference, Glasgow, 2000* (James & James, London, 2001), p. PA2.4.
[25]M. Birkholz, E. Conrad, and W. Fuhs, Jpn. J. Appl. Phys., Part 1 **40**, 4176 (2001).
[26]P. Reinig, F. Fenske, W. Fuhs, V. Alex, and M. Birkholz, J. Vac. Sci. Technol. A **20**, 2004 (2002).
[27]N. Fujimura, T. Nishihara, S. Goto, J. Xu, and T. Ito, J. Cryst. Growth **130**, 269 (1993).
[28]X. Jiang, C. L. Jia, and B. Szyska, Appl. Phys. Lett. **80**, 3090 (2002).
[29]M. Birkholz, B. Selle, F. Fenske, and W. Fuhs, Phys. Rev. B **68**, 205414 (2003).
[30]H. Bartzsch, P. Frach, and K. Goedicke, Surf. Coat. Technol. **132**, 244 (2000).
[31]P. J. Kelly, R. Hall, J. O'Brien, J. W. Bradley, P. Henderson, G. Roche, and R. D. Arnell, J. Vac. Sci. Technol. A **19**, 2856 (2001).
[32]M. Birkholz, U. Albers, and T. Jung, Surf. Coat. Technol. **179**, 279 (2004).
[33]K. Ishii, J. Vac. Sci. Technol. A **7**, 256 (1989).
[34]T. Jung and A. Westphal, Surf. Coat. Technol. **59**, 171 (1993).
[35]K. Ishii, T. Ohba, and T. Hara, Mater. Sci. Eng., A **217–218**, 232 (1996).
[36]T. Jung, T. Kälber, and V. von der Heide, Surf. Coat. Technol. **86–87**, 218 (1996).
[37]K. Ishii and H. Hamakake, in *43rd Annual Technical Conference of the Society of Vacuum Coaters, Denver, 2000* (Society of Vacuum Coaters, Albuquerque, NM, 2000), p. 107.
[38]M. Höfer, A. Jung, T. Jung, H.-U. Kricheldorf, and F. Schmidt, in *43rd Annual Technical Conference of the Society of Vacuum Coaters, Denver, 2000* (Society of Vacuum Coaters, Denver, 2000), pp. 287–292.
[39]J. A. Thornton, J. Vac. Sci. Technol. **11**, 666 (1974).
[40]M. Popeller and R. Abermann, Thin Solid Films **295**, 60 (1997).
[41]S. Machlin, *The Relationship Between Thin Film Processing and Structure* (Giro Press, Croton-on-Hudson, 1995), Chap. 6.
[42]C. Genzel, J. Appl. Crystallogr. **32**, 770 (1999).
[43]C. Genzel and W. Reimers, Z. Metallkd. **94**, 655 (2003).
[44]T. Göbel, S. Menzel, M. Hecker, W. Brückner, K. Wetzig, and C. Genzel, Surf. Coat. Technol. **142–144**, 861 (2001).
[45]T. Kälber, Doctoral thesis, TU Braunschweig, 1998.
[46]C. Genzel, Adv. X-Ray Anal. **44**, 247 (2001).
[47]K. Helming, *Texturapproximation durch Modellkomponenten* (Cuivillier Verlag, Göttingen, 1996).
[48]E. Macherauch and P. Müller, Z. Angew. Phys. **13**, 305 (1961).
[49]V. Hauk, *Structural and Residual Stress Analysis by Nondestructive Methods* (Elsevier, Amsterdam, 1997), pp. 344 and 400.
[50]J. D. Eshelby, Proc. R. Soc. London, Ser. A **241**, 376 (1957).
[51]E. Kröner, Z. Phys. **151**, 504 (1958).
[52]Landolt-Börnstein, *Zahlenwerte und Funktionen aus Naturwissenschaft und Technik*, Vol. 11 (Springer, Berlin, 1979).
[53]B. A. Movchan and A. V. Demchishin, Phys. Met. Metallogr. **28**, 83 (1969).
[54]J. A. Thornton, Annu. Rev. Mater. Sci. **7**, 239 (1977).
[55]P. B. Barna and M. Adamik, Thin Solid Films **317**, 27 (1998).
[56]G. K. Wehner, and G. S. Anderson, in *Handbook of Thin Film Technology*, edited by L. I. Maissel and R. Glang (McGraw-Hill, New York, 1983), pp. 3.1–3.38.
[57]C. Weißmantel and C. Haman, *Grundlagen der Festkörperphysik*, 3rd ed. (VEB Deutscher Verlag der Wissenschaften, Berlin, 1989).
[58]H. Windischman, Crit. Rev. Solid State Mater. Sci. **17**, 547 (1992).
[59]W. D. Nix and B. M. Clemens, J. Mater. Res. **14**, 3467 (1999).
[60]W. Kleber, H.-J. Bautsch, J. Bohm, and I. Kleber, *Einführung in die Kristallographie*, 17th ed. (Verlag Technik, Berlin, 1990).
[61]D. Gloaguen, M. Francois, R. Guillen, and J. Royer, Phys. Status Solidi A **193**, 12 (2002).
[62]J. H. Driver, in Proceedings of the 10th ICOTOM, Clausthal, 1993 Mater. Sci. Forum 157–162, Transtech. Publ., p. 585.
[63]A. D. Rollett and S. I. Wright, in *Texture and Anisotropy—Preferred Orientations in Polycrystals and their Effect on Materials Properties*, edited by U. F. Kocks, C. N. Tomé, and H.-R. Wenk (University Press, Cambridge, 1998), pp. 178–238.